Deriving L-Band Tilting Ocean Surface Roughness From Measurements by Operational Systems

Paul A. Hwang

***Abstract*— Waves much shorter than those measured by operational systems make significant contribution to the ocean surface roughness. This article describes a method to obtain the L-band tilting ocean surface roughness using wind speed and windsea dominant wave period coupled with a wind–wave spectrum model. Examples are presented with wind and dominant wave data from ocean buoys and hurricane hunters. Several related issues are discussed: high-frequency wave spectrum, integration limit, swell contribution, and measurements in extreme winds: 1) it is well known since the 1970s that with stationary sensors, extending the frequency range in measuring elevation spectrum does not yield useful short-wave information because of the low signal level and large Doppler frequency shift involved in measuring short waves. 2) Low-pass mean square slopes (LPMSSs) integrated to 5 and 11 rad/m are computed to quantify their difference as a function of wind speed and inverse wave age (IWA). The normalized difference decreases with increasing wind speed and decreasing IWA. 3) Swell contribution to the L-band LPMSS is almost negligible for wind speed greater than 5 m/s (less than 5% in 99% of observations). In low-wind conditions (wind speed less than 5 m/s), the swell contribution is difficult to assess because of inaccuracy in identifying the weak windsea system. 4) The coarse resolution in National Data Buoy Center (NDBC) wave spectra causes large data scatter in the computed LPMSS in very high winds (greater than 20 m/s). A mitigating solution is offered.**

***Index Terms*— Dominant wave period (DWP), ocean surface roughness, remote sensing, tropical cyclone (TC), wind speed.**

I. Introduction

OCEAN surface roughness is an important subject in remote sensing research. Forward computation of scattering and emission requires an accurate specification of the ocean surface roughness spectrum to obtain correct solutions. Despite the critical role it plays in ocean remote sensing, the research on the subject is sketchy. The number of direct measurements of ocean surface roughness remains small. All the reported data were collected in mild-to-moderately high-wind conditions (less than 15 m/s) and with limited geographic coverage [1]–[15]. In comparison, spaceborne remote sensing systems provide ocean surface roughness data in large quantity, under expansive environmental conditions, and with global coverage. For example, short waves in Bragg resonance length scales can be retrieved from the L-, C-, and Ku-band NRCS through the well-established geophysical model functions [16]–[18]. The procedure makes use of the dominance of Bragg resonance mechanism in vertical receive vertical transmit (VV) surface scattering over the incidence angle range between about 45° and 65°. Microwave scatterometers can, therefore, be treated as surface roughness spectrometers [19]. The L-, C-, and Ku-band NRCSs provide wavenumber resolution between about 30 and 510 rad/m, i.e., surface wave wavelengths between 20.9 and 1.23 cm.

For specular surface return, the critical surface roughness is the tilting ocean surface slope, which is a cumulative quantity with contribution by waves longer than about three times the Bragg resonance wavelength. For L-band, the contributing surface waves are longer than about 0.6 m and wave components in the neighborhood of the energetic spectral peak region make important contribution to the tilting roughness. Extensive ocean surface wave research has established that the surface wave energy sharply drops off from the spectral peak region toward both longer and shorter length scales [20]–[24]. Operational systems measuring ocean waves are designed to provide faithful data on the dominant wave properties such as significant wave height (SWH) H_s and dominant wave period (DWP) T_p. The upper limit frequency of reported surface wave spectrum is typically less than 0.5 Hz. Therefore, the shortest wavelength resolved by operational wave measurement systems is about 6 m at best, thus the spectrum leaves an order of magnitude big gap for providing the tilting roughness to support the L-band reflectometer remote sensing research.

This article discusses a method to extract the low-pass mean square slope (LPMSS) suitable for the L-band reflectometry by employing a wind–wave spectrum model with inputs that can be reliably supplied by an operational system. Section II gives a brief review of a general function of wind–wave spectral models established for ocean science and engineering applications. Section III describes the proposed approach to obtain the LPMSS using the general wind–wave spectral function with input from an operational system. The method is applied to two types of operational wind and wave measurements: National Data Buoy Center (NDBC) buoys and hurricane hunters. Section IV discusses issues such as extending the frequency range in the measurement system, sensitivity to the upper cutoff wavenumber for LPMSS integration, swell contribution, and measurements in extreme wind conditions. Section V provides the summary.

Manuscript received April 14, 2020; revised June 1, 2020; accepted June 6, 2020. Date of publication June 17, 2020; date of current version January 21, 2021. This work was supported by the Office of Naval Research under Grant N0001416WX00044.

The author is with the U.S. Naval Research Laboratory, Washington, DC 20375 USA (e-mail: paul.hwang@nrl.navy.mil).

Color versions of one or more of the figures in this article are available online at https://ieeexplore.ieee.org.

Digital Object Identifier 10.1109/TGRS.2020.3001023

II. Wind–Wave Spectrum Models

A. Spectral Functions

The appendix of [25] describes several major wind–wave spectrum models used by oceanographers, including Pierson and Moskowitz (PM or P) [20], Joint North Sea Wave Project (JONSWAP or *J*) [21], [22], Donelan *et al.* (*D*) [23], and Young (*Y*) [24]. These spectral models can be described by a general (G) spectrum function as follows [25]:

$$S(\omega) = \alpha g^2 \omega_{\rm p}^{-5} \varsigma^{-s_{\rm f}} \exp\left[-\frac{s_{\rm f}}{4}\varsigma^{-4}\right] \gamma^{\Gamma}$$
$$\Gamma = \exp\left[-\frac{(1-\varsigma)^2}{2\sigma^2}\right]; \quad \varsigma = \frac{\omega}{\omega_{\rm p}} \tag{1}$$

where ω is the angular frequency, g is the gravitational acceleration, $\omega_{\rm p}$ is the spectral peak frequency, α, γ, and σ are the spectral parameters, which are functions of spectral slope—$s_{\rm f}$ and wave development stage represented by the dimensionless peak frequency (DPF) $\omega_{\#} = \omega_{\rm p} U_{10}/g = U_{10}/c_{\rm p}$. The DPF is also the inverse wave age (IWA). For remote sensing application, the frequency spectrum can be converted to the wavenumber spectrum by $S(k)dk = S(\omega)d\omega$, where k is the wavenumber. Applying the deep-water gravity wave dispersion relation: $\omega^2 = gk$, then $S(k) = S(\omega)g/2\omega$.

Extensive wave research has established that the minimum value of $\omega_{\#}$ of a wind–wave system is about 0.8, that is, the dominant wave phase speed $c_{\rm p}$ in a wind-generated wave system is less than $1.25U_{10}$ [20]. The reason $c_{\rm p}$ can exceed U_{10} is because of nonlinear wave–wave interaction, which continues to produce spectral frequency downshift such that the dominant wave can outrun the wind speed, i.e., $c_{\rm p} > U_{10}$ [21]–[23]. Another reason is that the 10-m elevation of surface wind speed reference is somewhat arbitrary and it is chosen as a matter of convenience and necessity to have a common reference. If the wind speed at the elevation one-half the dominant wavelength $U_{\lambda/2}$ was chosen, $c_{\rm p}$ at maturity would have been close to one, i.e., waves reach maturity when their speed matches the reference speed of the wind field [26]. Theoretically, the dynamic wave perturbation decays exponentially and becomes negligible at a distance $\lambda/2$ away from the air–water surface. Defining waves reaching maturity as $c_{\rm p} = U_{\lambda/2}$ is, thus, physically more appealing. However, using $U_{\lambda/2}$ requires surface wave information that is unavailable in most cases.

There are two main differences among various spectrum models: $\omega_{\#}$ and $s_{\rm f}$.

1) *P* is for mature waves: $\omega_{\#} =\sim 0.8$, $s_{\rm f} = 5$.
2) *J* is for any wave age: $\omega_{\#} >\sim 0.8$, $s_{\rm f} = 5$.
3) *D* is for any wave age: $\omega_{\#} >\sim 0.8$, $s_{\rm f} = 4$.
4) *Y* is for any wave age: $\omega_{\#} >\sim 0.8$, $s_{\rm f}$ is variable. The three spectral coefficients α, γ, and σ in the *Y* model use those of *J* or *D* models, which are theoretically applicable only to $s_{\rm f} = 5$ or 4, respectively.
5) *G* is for any wave age: $\omega_{\#} >\sim 0.8$, $s_{\rm f}$ is variable. The three spectral coefficients α, γ, and σ are functions of $s_{\rm f}$ and $\omega_{\#}$. The spectral slope is determined to be a stochastic variable with Gaussian distribution and a mean value of about −4.5.

With the L-band LPMSS data from Global Positioning Reflectometry (GPSR) [27]–[30], a wind-dependence function of the mean value of stochastic $s_{\rm f}$ is derived as follows:

$$\langle s_{\rm f} \rangle = \begin{cases} s_1, & U_{10} \le U_1 \\ s_1 \, (U_{10}/U_1)^q, & U_{10} > U_1. \end{cases} \tag{2}$$

The parameter values $[s_1, U_1, q] = [4.7, 18, 1/8]$ are recommended in [31]. In the remainder of this article, the angular brackets are dropped and the notation $s_{\rm f}$ is understood to be the mean value of the stochastic variable. The *G* spectrum with $s_{\rm f}$ defined by (2) is referred to as the G18 spectrum model. The G18 spectrum model serves as the foundation of this article for addressing several practical issues encountered in using measurements derived from operational systems such as NDBC buoys, which have been an important data source of remote sensing calibration/validation effort.

B. Wave Height and Wave Slope

Here, the properties of wind–wave spectrum are analyzed in order to gain a better insight for developing a method to obtain the LPMSS from measurements of operational systems such as the wind and wave data from ocean buoys or hurricane hunters. For ocean science and engineering applications, the primary purpose of a wave spectrum model is to characterize correctly the energetic portion of the wind-generated surface waves. One robust relationship connecting the three integral properties of a wind–wave system is the power function relating the dimensionless wave variance and DPF $\eta_{\#}$–$\omega_{\#}$:

$$\eta_{\#} = R\omega_{\#}^{r}. \tag{3}$$

The total energy per unit area, E (in J/m^2), of a random wave field is $E = \rho_w g \eta_{\rm rms}^2$ [32], [33], where $\eta_{\rm rms}^2$ is the variance of surface displacement and $\rho_{\rm w}$ is the water density. Because $\rho_{\rm w}$ and g are essentially constant for surface wave analysis (about 1024 kg/m^3 and 9.8 m/s^2, respectively), the dimensionless variance of surface elevation $\eta_{\#} = g^2\eta_{\rm rms}^2/U_{10}^4$ is also referred to as the dimensionless wave energy. Leaving the dimensional variables explicitly in (3), the similarity function connects the three important parameters of a windsea system: U_{10}, $H_{\rm s}$, and $T_{\rm p}$; $H_{\rm s} = 4\eta_{\rm rms}$, and $T_{\rm p} = 2\pi/\omega_{\rm p}$

$$\left(\frac{g^2 H_{\rm s}^2}{16 U_{10}^4}\right) = R\left(\frac{U_{10} 2\pi}{g T_{\rm p}}\right)^r. \tag{4}$$

Fig. 1 shows the examples of field measurements adhering to the similarity function. The data include five fetch-limited wave-generation experiments under steady wind forcing conditions (BHDDB, representing the initials of the lead authors in the five publications in chronological order) [21], [23], [34]–[36], an air–sea interaction experiment (IntOA) under mountain gap wind conditions with wind speed rising and falling rapidly [37]–[39], and hurricane hunter wind and wave measurements inside tropical cyclone (TC) Bonnie 1998 (B24) [40]–[42]. Despite the incredibly different wind forcing conditions, ideal quasi-steady and homogenous winds in fetch-limited experiments, unsteady rising and falling mountain gap winds in IntOA, and obviously inhomogeneous and

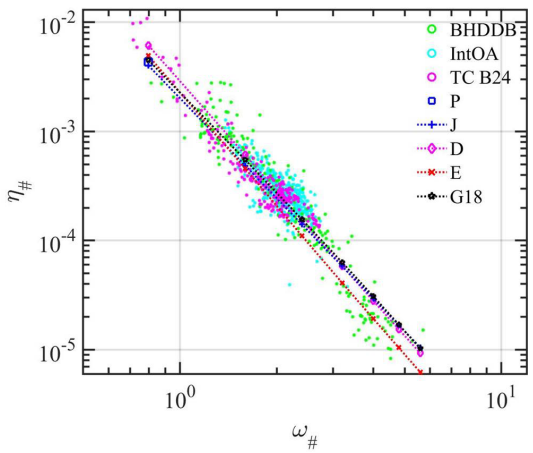

Fig. 1. Similarity relation connecting the three integral properties of wind–wave systems: U_{10}, H_s, and T_p expressed as $\eta_\#(\omega_\#)$ obtained by different wind–wave spectrum models (smooth curves as labeled in the legend). Superimposed in the background are field measurements in steady fetch-limited wave growth experiments (BHDDB), unsteady mountain gap wind conditions (IntOA), and inside TC Bonnie 1998 (TC B24). More detail is described in the text.

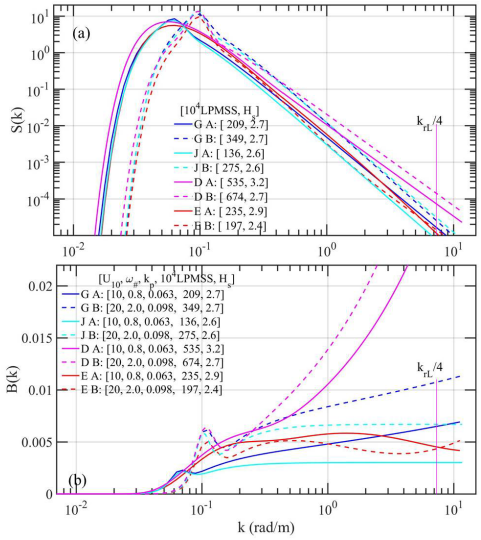

Fig. 2. Examples of (a) $S(k)$ and (b) $B(k)$ computed for two different (U_{10}, $\omega_\#$) combinations with J, D, G, and E spectrum models.

chaotic winds inside TCs, the $\eta_\#(\omega_\#)$ results are basically indistinguishable.

Superimposed on the data clouds are $\eta_\#(\omega_\#)$ computed from wind–wave spectrum models described in Section II-A: J, D, and $G18$. The agreements between different models and field data are almost identical. The result computed by the E spectrum model [43] is also included in Fig. 1 with a red curve. The E-model is employed in the Cyclone Global Navigation Satellite System (CYGNSS) program [44]. The long-wave portion of the E-model is based on a modified Donelan–Pierson spectrum [45]. Although the E result of $\eta_\#(\omega_\#)$ differs somewhat from the other models, its agreement with field data is not any worse than the J, D, and $G18$ models.

Fig. 2(a) and (b) shows the two examples of the wave elevation spectra $S(k)$ and the dimensionless spectra $B(k) = k^3 S(k)$ computed with the J, D, E, and $G18$ models, respectively. Case A is a mature windsea ($\omega_\# = 0.8$) at $U_{10} = 10$ m/s, and case B is a relatively young windsea ($\omega_\# = 2.0$) at $U_{10} = 20$ m/s. The spectral peak wavenumber of the low-wind mature sea is 0.063 rad/m, which is lower than that of the higher wind but younger sea at 0.098 rad/m, i.e., the dominant wavelength of the low wind Case A is longer than that of the high wind Case B. This illustrates the importance of considering the wave development stage in addition to wind speed in discussing the wind-generated wave spectrum.

The energy spectral density of a wind–wave system, $S(k)$, sharply drops off from the peak region toward both longer and shorter wavelength components [Fig. 2(a)]. The wave energy is, thus, contributed primarily by the wave components near the spectral peak region. Contrary to the wave energy or surface elevation, the surface slope $\nabla\eta$ is proportional to the product of wavenumber and surface elevation. The weighting by wavenumber shifts the relative contribution toward the short-scale waves. The LPMSS $s^2_{k_u}$ is the integration of slope spectrum $k^2 S(k)$:

$$s^2_{k_u} = \int_0^{k_u} k^2 S(k) dk = \int_0^{k_u} B(k) d \ln k \tag{5}$$

where k_u is the upper bound of integration. In Fig. 2(b), the semilogarithmic $B(k)$ plot describes the contributions to the surface mean square slope by individual wavenumber components. In Fig. 2(b), the integrated LPMSS $s^2_{k_u}$ and SWH H_s are tabulated; the upper and lower bounds of integration are 0.001 and 7.5 rad/m, respectively. For these two cases, the integrated surface elevation variances are almost identical. The SWHs computed with the four spectrum models for the two cases are in agreement with each other to within about 20%. On the other hand, the LPMSSs integrated to 7.5 rad/m ($s^2_{7.5}$) obtained from the four spectrum models may differ by a factor of two or more. As shown in Fig. 2(b), the difference in the LPMSS results is mainly contributed by the region with wavenumber higher than about two to three times the spectral peak value.

The elevation and slope analysis provide some insight on the design of methods to obtain the LPMSS from operational system measurements. Similar to the wave spectrum models, the operational wave measurement systems aim to provide the best representation of the dominant wave properties such as H_s and T_p. Because short-scale waves make negligible contribution to the wave energy or elevation, these operational systems cannot be expected to provide accurate measurements of short-wave properties, despite their important contribution to the ocean surface slope. From this understanding, the dominant wave properties are the more reliable output from the operational ocean wave measurement systems. Employing a wave spectral model that makes use of the more reliable dominant wave properties offers a better chance for deriving the LPMSS from operational measurements. This approach differs from the conventional and apparent choice of trying to extrapolate the measured spectrum toward higher wave frequency or wavenumber by appending a spectral tail. The extrapolation approach is not recommended because of the fact that the high-frequency region in the operational spectrum output is the least reliable, due to its low signal-to-noise ratio (SNR) and increasing distortion by the Doppler frequency

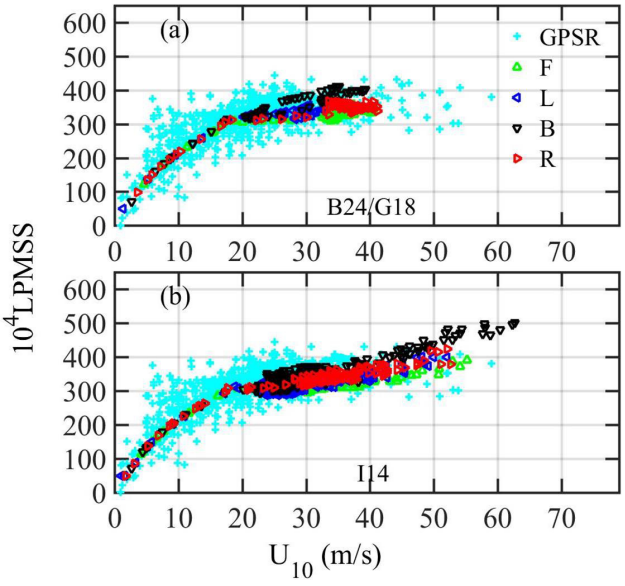

Fig. 3. LPMSS computed with the G18 spectrum model using the hurricane hunter wind speed and DWP data. (a) B24. (b) I14. The LPMSS derived from GPSR is illustrated in the background for comparison. The hurricane hunter results are sorted into four quarters with respect to the TC heading (F, L, B, and R for front, left, back, and right, respectively).

shift toward shorter waves. This point is further explained in Section IV-A.

III. LPMSS From Operational Measurements

A. Hurricane Hunter

Measuring waves inside a TC is challenging. The data obtained by scanning radar altimeter (SRA) or wide-swath SRA (WSRA) carried on hurricane hunters are the most reliable to this date. Four of the SRA data sets have been extensively examined [40]–[42], [46]–[50]. These four data sets are obtained in Bonnie 1998 (B24) and Ivan 2004 (I09, I12, and I14). For the spectral models (J, D, E, and $G18$) described in Section II, the spectrum is uniquely determined by U_{10} and T_p; therefore, the LPMSS can be computed with U_{10} and T_p as the only input [31], [51].

Fig. 3 shows the two examples of $s^2_{7.5}$ computed by the G18 spectrum model with the hurricane hunter U_{10} and T_p data. For comparison, illustrated in the background is the LPMSS derived from GPSR (denoted by s^2_{GPS}) [27]–[30]. The hurricane hunter wind and wave data include precise information of the measurement location with respect to the TC center for examining the radial and azimuthal variation of the wind and wave properties. The results presented in Fig. 3 are sorted into four quarters with respect to the TC heading (F, L, B, and R for front, left, back, and right, respectively). For a given wind speed, the highest LPMSS is usually found in the back quarter and the lowest is in the front quarter.

B. NDBC Buoy

Most of the *in situ* simultaneous ocean wind and wave data are from meteorological buoys (MetBuoy). The U.S. National Data Buoy Center (NDBC) maintains several dozens

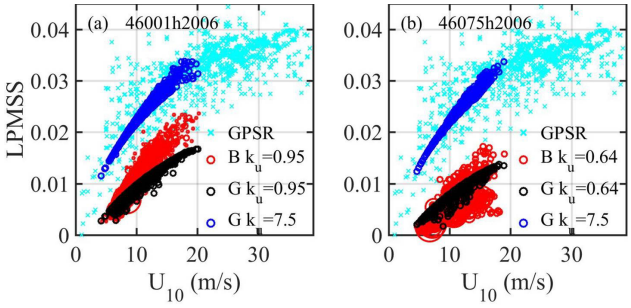

Fig. 4. Examples of obtaining the LPMSS from the G18 spectrum model using NDBC buoy wind speed and windsea DWP data. (a) Buoy 46001 at Western Gulf of Alaska—175 nm SE of Kodiak, Alaska, during 2006, f_{max} = 0.485 Hz. (b) Buoy 46075 at Shumagin Islands—85 nm South of Sand Point, Alaska, during 2006, $f_{max} = 0.4$ Hz. In the legend, B is buoy, and G is the G18 wave spectrum model.

of MetBuoys in both east and west U.S. continental coasts, around Hawaii islands, and along the equator. These buoys typically make hourly recording of the wind velocity, wave spectrum, and other meteorological and oceanographic observations such as air and water temperatures. Some wave spectra are reported with 47 spectral components in frequency (f) range between 0.02 and 0.485 Hz, corresponding to $k = 0.0016$ and 0.95 rad/m, respectively. Some spectra have 38 spectral components between 0.03 and 0.4 Hz, corresponding to $k = 0.0036$ and 0.64 rad/m. The first step of using the MetBuoy spectrum is to separate the windsea and swell components of the measured wave spectrum. The results presented in this article employ the spectrum integration method described in [52]. The LPMSS is computed from the wind–wave spectrum models using wind speed and windsea spectrum peak frequency as input. To compare with the buoy measurement, the model LPMSS is from integration to $k_u = 0.95$ or 0.64 rad/m, i.e., $s^2_{0.95}$ or $s^2_{0.64}$, corresponding to the maximum buoy spectrum frequency of 0.485 or 0.4 Hz. For L-band, the LPMSS is integrated to a representative $k_u = 7.5$ rad/m, i.e., $s^2_{7.5}$.

Fig. 4 shows the two examples of obtaining the LPMSS from the G18 wind–wave spectrum model using NDBC buoy wind speed and windsea DWP data. The red and black markers in Fig. 4(a) and (b) are the measured and modeled $s^2_{0.95}$ and $s^2_{0.64}$, respectively. The modeled $s^2_{0.95}$ and $s^2_{0.64}$ are in reasonably good agreement with the buoy data, which show somewhat steeper increasing trend with wind, especially for the wave spectrum with $f_{max} = 0.485$ Hz. Further discussion on the high-frequency wave spectrum is given in Section IV-A. $s^2_{7.5}$ computed with the G18 model (blue markers) compares well with s^2_{GPS} (cyan markers).

IV. Discussion

A. High-Frequency Measurement

High-frequency wave spectrum measurements are frequently obtained in ocean research experiments in the open ocean. As an example, 20-Hz sampling is used for wave measurement by thin wire gauges mounted on a spar buoy in IntOA. The measurement location is 22-km offshore with

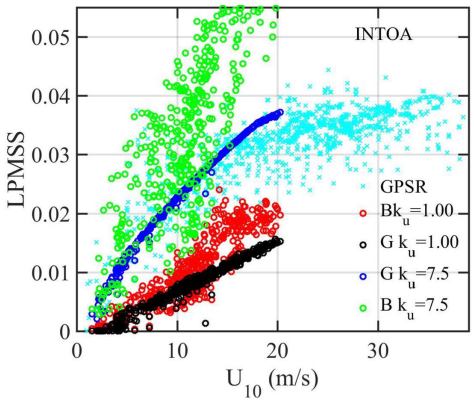

Fig. 5. LPMSS computed from high-frequency-resolution wave spectra measured by thin wires mounted on a spar buoy during IntOA experiment, integrated to $k_u = 1$ and 7.5 rad/m, and comparison with the results obtained by the G18 spectrum model and GPSR.

60-m water depth in Gulf of Tehuantepec, Mexico [37]–[39]. The data provide wave spectral resolution with maximum frequency $f_{max} = 10$ Hz or equivalently $k_{max} = 264$ rad/m.

Fig. 5 shows the LPMSSs integrated to $k_u = 1$ and 7.5 rad/m and their comparison with the G18 spectrum model and GPSR measurements. For the $k_u = 1$ rad/m results, the agreement between the field data and G18 model is very good up to about 13 m/s wind speed, beyond which the measured result is much larger than the G18 model. For the measured LPMSS integrated to $k_u = 7.5$ rad/m (green circles), the scatter is rather large and the magnitude is obviously too large compared to s^2_{GPS} for U_{10} greater than about 10 m/s.

Making measurement of short waves in the ocean is a complicated problem. Although extending the measurement toward higher frequency is an apparent solution, such an approach has proved to be unsatisfactory as illustrated by the IntOA example. The fact that short-scale-wave properties cannot be reliably obtained from high-frequency wave elevation measurement by stationary devices is well known to experimentalists since the 1970s or earlier. This is because of the surface-current-induced Doppler frequency becoming increasingly more severe toward shorter wavelengths. Furthermore, the sharp drop-off of the surface wave elevation spectrum [Fig. 2(a)] means poor SNR of the short-scale wave spectral signal, which can be easily swamped by the system noise or the spectral leakage from the dominant wave region where the spectral density is many orders of magnitude larger. Attempts to characterize short waves with wavelengths in the microwave Bragg resonance scales have been conducted with wave slope sensing techniques instead of elevation sensing to increase the SNR of short waves [1]–[15]. Performing spatial measurements to obtain the wavenumber spectrum directly or conducting free-drifting Lagrangian measurements can also alleviate the Doppler frequency shift problem that distorts the high-frequency portion of the measured spectrum [12]–[15].

B. Upper Bound of LPMSS Integration

The upper-bound wavenumber k_u for LPMSS integration is determined by the microwave wavenumber k_r and

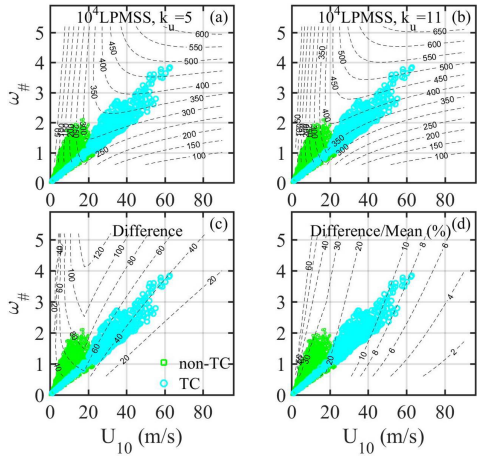

Fig. 6. Contour lines showing (a) LPMSS integrated to $k_u = 5$ rad/m, (b) LPMSS integrated to $k_u = 11$ rad/m, (c) difference between LPMSSs integrated to $k_u = 11$ and 5 rad/m, and (d) difference between LPMSSs integrated to $k_u = 11$ and 5 rad/m normalized to their mean, in percent. The cyan and green markers show the typical ω#(U10) observed in TC and non-TC conditions.

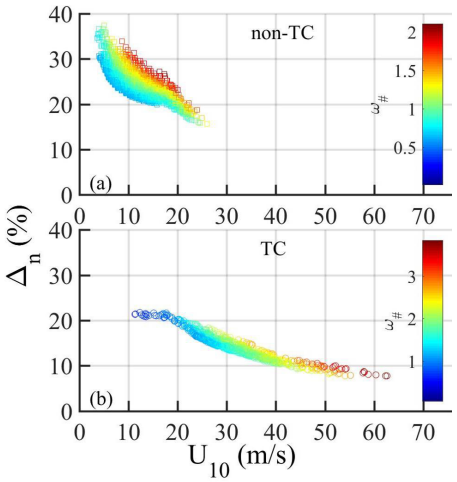

Fig. 7. Normalized difference of the LPMSS calculated with $k_u = 11$ and 5 rad/m. (a) Non-TC conditions. (b) Inside TCs.

incidence angle θ. For altimeter, the frequently used range is $k_u = k_r/3$ to $k_r/5$. For CYGNSS using GPS L1 frequency (1.575 GHz), $k_r = 33$ rad/m, thus the altimeter range of $k_u = 11$–6.6 rad/m. The contour lines in Fig. 6(a) and (b) show the LPMSSs computed from the G18 spectrum model with $k_u = 5$ and 11 rad/m (s^2_5 and s^2_{11}), respectively, as functions of U_{10} and $\omega_\#$. The difference between s^2_5 and s^2_{11} is given in Fig. 6(c), and the difference normalized by the mean $\Delta_n = (s^2_{11} - s^2_5)/[(s^2_5 + s^2_{11})/2]$ in percentage is given in Fig. 6(d). Plotted in the background with cyan and green markers is the typical $\omega_\#(U_{10})$ observed in TC and non-TC conditions, respectively.

Using these $\omega_\#(U_{10})$ observations, the normalized difference Δ_n can be estimated for non-TC and TC conditions (Fig. 7). There is a trend of decreasing Δ_n with increasing wind speed, reflecting the downshift of spectral peak with increasing wind for the same wave age. For the same

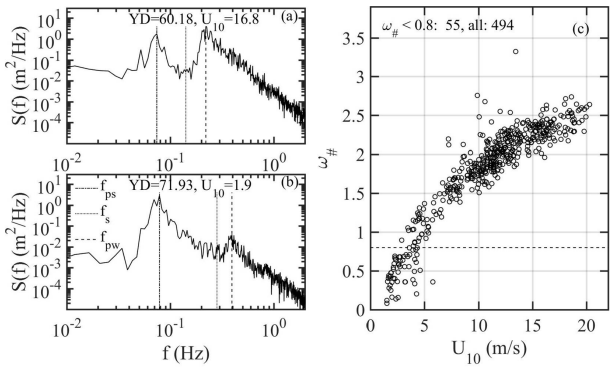

Fig. 8. Two examples of the bimodal spectra observed during IntOA. (a) $U_{10} = 16.8$ m/s. (b) $U_{10} = 1.9$ m/s. The swell and windsea spectral peak frequencies and the separation frequency are marked by vertical lines. (c) Observed $\omega_{\#}(U_{10})$ of the windsea portion of the spectrum. Failure to separate swell and windsea causes $\omega_{\#} < 0.8$, and it usually occurs in low winds.

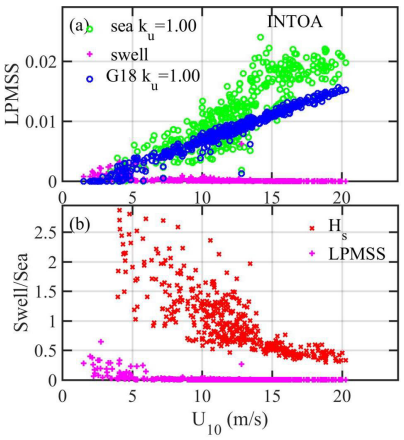

Fig. 9. (a) LPMSS of swell and windsea integrated to $k_u = 1$ rad/m. (b) H_s and LPMSS ratios of swell to sea.

wind speed, Δ_n decreases as waves develop from young to mature stage (decreasing $\omega_{\#}$), again reflecting the downshift of spectral peak from young to mature stage. For non-TC conditions [Fig. 7(a)], the range of Δ_n is about 22 and 32% at $U_{10} = 10$ m/s, and it drops to about 18% and 22% at $U_{10} = 20$ m/s. For $U_{10} \leq \sim 5$ m/s, it is difficult to obtain the correct windsea spectral peak frequency and the LPMSS estimation in low wind is less reliable. Inside TCs [Fig. 7(b)], Δ_n decreases from about 20% at 20 m/s, to about 10% at 50 m/s, with a small range of variation for the observed range of $\omega_{\#}$. In the hurricane hunter data sets analyzed in this article, measurement locations of $U_{10} \leq \sim 20$ m/s are within 20 km from the hurricane center. The wave condition is windsea mixed with strong swell and the determination of the windsea peak frequency from the measured spectrum is not accurate as reflected in the resulting $\omega_{\#}$ showing values much smaller than 0.8.

C. Swell Contribution

Ocean waves are mostly composed of multiple wave systems of local windsea mixed with swells from distance storms propagated to the measurement location. Only the windsea portion of the spectrum maintains a high correlation with the local wind for remote sensing wind retrieval. To extract the tilting wind-induced surface slope, the windsea and swell systems need to be separated. Fig. 8(a) and (b) shows the two examples (high and low winds) of the multimodal spectra and the swell-sea separation results using the spectrum integration method [52]. The windsea and swell spectral peak frequencies, f_{pw} and f_{ps}, respectively, and the swell-sea separation frequency f_s are illustrated in Fig. 8(a) and (b) with vertical lines. In low winds, the local windsea spectrum may be too weak and overwhelmed by the swell, causing difficulty in detecting the windsea spectral peak. For example, in the low-wind case ($U_{10} = 1.9$ m/s) shown in Fig. 8(b), $f_{pw} = 0.4$ Hz is determined by the swell-sea separation method. The corresponding phase speed is 3.9 m/s and $\omega_{\#} = 0.49$, which is much lower than the expected minimum value of 0.8 for a windsea system. This detected f_{pw} at 0.4 Hz is a residual wave system from the earlier higher winds. The true local sea is the little bump near 0.8 Hz ($\omega_{\#} = 1.03$) that is too weak to be detected by the swell-sea separation method employed in this article.

Fig. 8(c) shows the scatter plot of $\omega_{\#}(U_{10})$ of the full set of IntOA observations constituting 494 spectra, 55 of which resulting in $\omega_{\#} < 0.8$ and indicating that the swell-sea separation failed to detect the correct windsea spectral peaks. Of the 55 failed cases, 54 are in low winds with $U_{10} < 5$ m/s.

The minimum frequency f_{min} of the IntOA spectrum is 3.06×10^{-3} Hz, which corresponds to $k_{min} = 3.76 \times 10^{-5}$ rad/m. Fig. 9(a) shows the LPMSS integrated from k_{min} to 1 rad/m (i.e., s_1^2) in green. The swell-only LPMSS integrated from k_{min} to k_s (i.e., $s_{k_s}^2$) is shown in magenta, where k_s is the wavenumber corresponding to the sea-swell separation frequency f_s. Except in low-wind conditions ($U_{10} < 5$ m/s), $s_{k_s}^2 \ll s_1^2$. As discussed in Fig. 8(c), there is difficulty in separating swell and windsea in conditions with U_{10} less than about 5 m/s.

Fig. 9(b) shows the swell to windsea ratio of SWH H_{ss}/H_{sw} with red markers and the corresponding ratio of the L-band LPMSS ($s_{k_s}^2/s_{7.5}^2$) with magenta markers, where $s_{7.5}^2$ is computed with the G18 spectrum model. Swell presence is always prominent in IntOA. For $U_{10} < 5$ m/s (78 cases out of 494 total), $H_{ss}/H_{sw} > 1.4$ but $s_{k_s}^2/s_{7.5}^2$ remains less than 0.5 except for one case at $U_{10} = 2.6$ m/s. For $U_{10} > 5$ m/s (416 cases), $s_{k_s}^2/s_{7.5}^2$ is less than 0.03 in 406 cases (97.6%) and less than 0.05 in 412 cases (99.0%).

D. Very High-Wind Conditions

High winds are minor occurrences in long-term recordings. Two examples of yearlong NDBC records are presented here. Fig. 10(a) and (b) shows the results from buoy 46035 during 2006 and buoy 42003 during 2005, respectively. Station 46035 is at central Bering Sea, 310 nm North of Adak, Alaska. Out of 8638 spectra in the yearlong record, 93 have U_{10} greater than 20 m/s. Station 42003 is at east Gulf of Mexico, 208 nm West of Naples, Florida. The yearlong record contains 11 spectra with U_{10} greater than 20 m/s; all are caused by Hurricane Katrina. These 11 very

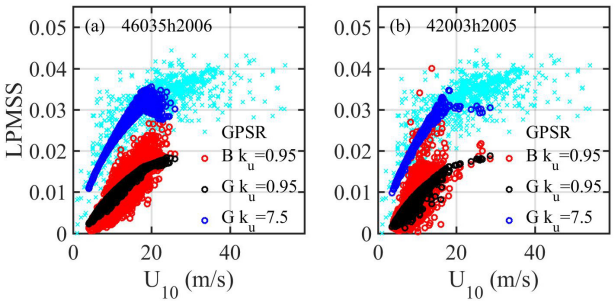

Fig. 10. High-wind examples of the LPMSS from the G18 wind–wave spectrum model using NDBC buoy wind and wave data. (a) Buoy 46035 at central Bering Sea, 310 nm North of Adak, Alaska, during 2006. (b) Buoy 42003 at East Gulf of Mexico, 208 nm West of Naples, Florida, during 2005 with Hurricane Katrina passing through the region. In the legend, B is buoy, and G is the G18 wave spectrum model.

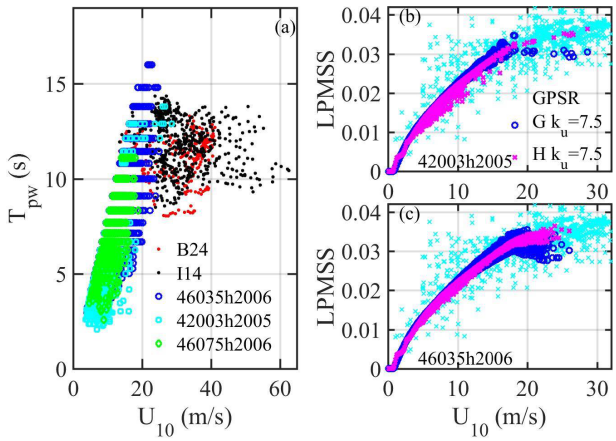

Fig. 11. (a) Scatter plot of $T_{\rm pw}$ versus U_{10} illustrating the coarse resolution of the buoy spectra. For comparison, the results from two Hurricane Hunter missions (B24 and I14) are superimposed in the background. (Right) Results of $s^2_{7.5}$ computed with the G18 and H18 spectrum models and their comparison with GPRS data for (b) buoy 42003 and (c) buoy 46035.

high-wind cases occurred during August 27, 2005, 18:00–August 28, 2005, 05:00 UTC. After which time, the sensors stopped functioning and records between August 28, 2005, 06:00 and October 6, 2005, 22:00 UTC are missing, resulting in 7144 spectra for the year.

Fig. 10(a) and (b) shows the comparison of $s^2_{0.95}$ calculated from the measured spectra and G18 spectrum model and $s^2_{7.5}$ by the G18 model and $s^2_{\rm GPS}$. The comparison between buoy and G18 $s^2_{0.95}$ is similar to that shown in Fig. 4(a). There is good agreement between $s^2_{7.5}$ and $s^2_{\rm GPS}$ with the exception for those cases with $U_{10} > 20$ m/s, for which the G18 computations using buoy U_{10} and $T_{\rm pw}$ input show a decreasing or flattening trend with increasing wind in both data sets.

A feasible explanation of the peculiar $s^2_{7.5}$ result in very high wind computed with the buoy U_{10} and $T_{\rm pw}$ input is attributable to the coarse frequency resolution of the buoy spectrum. Fig. 11(a) shows the windsea spectral peak period $T_{\rm pw}$processed from the buoy spectra measured at stations 42003, 46035, and 46075; only those data with $\omega_{\#} > 0.8$ are displayed. As discussed earlier in Section II, the most common NDBC wave spectra are reported with 47 components between 0.02 and 0.485 Hz or 38 components between 0.03 and 0.4 Hz. The former range applies to stations 42003 and 46035, and the latter range applies to station 46075. The relatively small number of spectral components yields coarse resolution of $T_{\rm pw}$. For comparison, the corresponding results from two hurricane hunter missions (B24 and I14) are superimposed in the background with red and black dots. The SRA 2-D wavenumber spectra are stored as 65×65 matrices with spectral resolution $dk = 0.0035$ rad/m, and the $k_{\rm max}$ of 1-D wavenumber spectra calculated with the archived data is 0.11 rad/m; the corresponding maximum angular frequency $\omega_{\rm max}$ is 1.04 rad/s or $f_{\rm max} = 0.17$ Hz. The quality of discriminating the spectral peak frequency is clearly much better in the hurricane hunter data sets compared to those in the NDBC buoy data sets.

$T_{\rm pw}$ is an important variable in quantifying the wind–wave spectrum (1), which is used to obtain the LPMSS. The coarse resolution of $T_{\rm pw}$ in the NDBC buoy data sets is likely the source of large $s^2_{7.5}$ data scatter shown in Fig. 10 in very high winds (blue circles). To preserve the monotonic wind speed dependence, the hybrid spectrum model H18 can be considered [51]. H18 employs the long-wave portion of G18 and the short-wave portion of H15 [53], with a linear transition in the wavenumber range between 1 and 4 rad/m. Fig. 11(b) and (c) shows $s^2_{7.5}$ computed by G18 and H18 for 42003 and 46035 data sets, and their comparison with $s^2_{\rm GPS}$. The logarithmic wind speed dependence is preserved in the H18 results. This is caused by the lack of wave age dependence in the short-wave portion of the H15 roughness spectrum by design [51], [53]. The data scatter due to coarse $T_{\rm pw}$ discrimination is, therefore, alleviated in the H18 results combining the G18 and H15 models.

E. Wind Direction and Other Factors

In many microwave remote sensing computations, it is of interest to know the directional distribution of the ocean surface roughness. Extensive research on the directional distribution of wind-generated waves has been reported [23], [54]–[59]. A summary discussion of various distribution functions can be found in the Appendix of [59]. The shortest wavelength in those reports is about 13 m. Reliable directional information of waves in the decimeter to decameter range is still lacking. The artificial slick data set of Cox and Munk [1] remains the most comprehensive field measurements of the LPMSS with crosswind and upwind resolution. Through the application of artificial slicks, they were able to acquire data in wind speeds between 2 and 11 m/s. The crosswind–upwind MSS ratio shows a logarithmic dependence on U_{10} with the magnitude in the measurements distributed over a narrow range between about 0.75 and 1.03. Extrapolation of their data shows that isotropic distribution of the LPMSS is reached at wind speed about 18 m/s [31].

The discussion of this article has been focused on deep water applications only. Other factors such as bathymetry (shoaling) and current straining at the boundary of major current systems or internal waves may also modify the surface

wave spectrum. There are many publications addressing such issues. Below is a short list for readers interested in the subjects [2], [3], [60]–[65].

V. Summary

Wind and wave measurements from operational systems such as NDBC buoys are an important data source for remote sensing calibration and validation effort. The wave spectra reported by NDBC buoys provide relatively coarse frequency resolution with maximum frequency less than 0.5 Hz. The shortest wavelength resolved in the spectrum is about one order of magnitude too long for providing the L-band reflectometry LPMSS reference. Because the high-frequency portion of the measured spectrum is more distorted, the recommended method to obtain the LPMSS is by employing the G18 or H18 spectrum model. It makes use of the more reliable windsea DWP and disregards the less reliable high-frequency portion. Several yearlong NDBC buoy data sets and four sets of hurricane hunter wind and wave measurements are used to test the efficacy of the method. The integrated L-band LPMSSs are in good agreement with those obtained by GPSR.

Several related issues are also discussed in this article. The conclusions are summarized as follows.

1) It is emphasized that attempts to extract short-wave properties from extending the frequency range in elevation spectrum measurements by stationary sensors have been demonstrated to be unproductive and well known since the 1970s or earlier. The main reasons are the low SNR and large Doppler frequency shift involved in the short-wave measurement. To increase the SNR, short-wave measurements are generally obtained with slope sensing techniques. Spatial measurements and free-drifting devices can alleviate the Doppler frequency distortion in the short-wave region (Section IV-A).
2) LPMSSs integrated to $k_u = 5$ and 11 rad/m are computed to discuss the effect of integration upper bound (Figs. 6 and 7). The normalized difference between $k_u = 5$ and 11 rad/m as a function of U_{10} and $\omega_\#$ is quantified with representative $\omega_\#(U_{10})$ observations in TC and non-TC conditions. The normalized difference decreases with increasing U_{10} and decreasing $\omega_\#$. In the examined TC data sets, the range is between about 19% and 20% at $U_{10} = 20$ m/s, and between 9% and 10% at $U_{10} = 50$ m/s. Below 20 m/s, it is difficult to determine the accurate windsea DWP and the LPMSS determination is less reliable. In non-TCs, the range is between about 25% and 35% at $U_{10} = 5$ m/s, and between 18% and 23% at $U_{10} = 20$ m/s. Below 5 m/s, it is difficult to determine the accurate windsea DWP and the LPMSS determination is less reliable.
3) Swell contribution is examined with a data set obtained in IntOA conducted in a location with prevailing swell presence. The waves are measured with high-frequency-response wire gauges mounted on a spar buoy and sampled at 20 Hz. The resulting spectra are of fine frequency resolution with 10-Hz maximum frequency. The contribution by swell to the L-band LPMSS is almost negligible for $U_{10} \geq 5$ m/s (less than 3% in 97.6% of cases and less than 5% in 99.0% of cases). In low-wind conditions ($U_{10} < 5$ m/s), the swell contribution is difficult to assess due to uncertainty in windsea identification.
4) In very high winds ($U_{10} > 20$ m/s), the coarse resolution of NDBC buoy spectra causes large data scatter in $s^2_{7.5}$ computed by the G18 spectrum model. The problem can be alleviated by using the H18 $s^2_{7.5}$.

Acknowledgment

U.S. Naval Research Laboratory Publication Number JA/7260—20-0635. The authors would like to thank the data provided by NOAA National Data Buoy Center (NDBC), Bay St. Louis, MS, USA, (https://www.ndbc.noaa.gov/station_history.php?station=46035; https://www.ndbc.noaa.gov/station_history.php?station=46001; https://www.ndbc.noaa.gov/station_history.php?station=46075; and https://www.ndbc.noaa.gov/station_history.php?station=46003). The hurricane hunter wind and wave data sets are deposited at https://www.researchgate.net/publication/325103857_EdWalshSRA_Ed_Walsh_collected_all_the_data_but_I_had_to_add_my_name_in_the_author_list_in_order_to_deposit_the_data_for_preservation. The IntOA data were provided by Héctor García-Nava and Francisco Ocampo-Torres.

References

[1] C. Cox and W. Munk, "Statistics of the sea surface derived from sun glitter," *J. Marine Res.*, vol. 13, no. 2, pp. 198–227, Feb. 1954.
[2] B. A. Hughes and H. L. Grant, "The effect of internal waves on surface wind waves 1. Experimental measurements," *J. Geophys. Res.*, vol. 83, no. C1, pp. 443–454, Jan. 1978.
[3] B. A. Hughes, "The effect of internal waves on surface wind waves 2. Theoretical analysis," *J. Geophys. Res.*, vol. 83, no. C1, pp. 455–465, Jan. 1978.
[4] S. Tang and O. H. Shemdin, "Measurement of high frequency waves using a wave follower," *J. Geophys. Res., Oceans*, vol. 88, no. C14, pp. 9832–9840, Nov. 1983.
[5] D. R. Thompson, B. L. Gotwals, and R. E. Sterner, II, "A comparisons of measured surface-wave spectral modulations with predictions from a wave-current interaction model," *J. Geophys. Res.*, vol. 93, no. C5, pp. 12339–12343, May 1988.
[6] O. H. Shemdin and P. A. Hwang, "Comparison of measured and predicted sea surface spectra of short waves," *J. Geophys. Res.*, vol. 93, no. C11, pp. 13883–13890, Nov. 1988.
[7] O. H. Shemdin, H. M. Tran, and S. C. Wu, "Directional measurement of short ocean waves with stereophotography," *J. Geophys. Res.*, vol. 93, no. C11, pp. 13891–13901, Nov. 1988.
[8] P. A. Hwang and O. H. Shemdin, "The dependence of sea surface slope on atmospheric stability and swell conditions," *J. Geophys. Res.*, vol. 93, no. C11, pp. 13903–13912, Nov. 1988.
[9] J. C. West, P. A. Hwang, R. K. Moore, J. C. Holtzman, and O. H. Shemdin, "The modulation of a radar signal from the ocean surface due to slope and hydrodynamic effects," *J. Geophys. Res.*, vol. 95, no. C9, pp. 16291–16297, Sep. 1990.
[10] S. J. Miller and O. H. Shemdin, "Measurement of the hydrodynamic modulation of centimeter waves," *J. Geophys. Res., Oceans*, vol. 96, no. C2, pp. 2749–2759, Feb. 1991.
[11] D. R. Thompson and B. L. Gotwals, "Comparisons of model predictions for radar backscatter amplitude probability density functions with measurements from SAXON," *J. Geophys. Res.*, vol. 99, no. C5, pp. 9725–9739, May 1994.
[12] P. A. Hwang, S. Atakturk, M. Sletten, and D. B. Trizna, "A study of the wavenumber spectra of short water waves in the ocean," *J. Phys. Oceanogr.*, vol. 26, no. 7, pp. 1266–1285, Jul. 1996.

[13] C. J. Zappa, M. L. Banner, H. Schultz, A. Corrada-Emmanuel, L. B. Wolff, and J. Yalcin, "Retrieval of short ocean wave slope using polarimetric imaging," *Meas. Sci. Technol.*, vol. 19, no. 5, May 2008, Art. no. 055503, doi: 10.1088/0957-0233/19/5/055503.

[14] C. J. Zappa *et al.*, "An overview of sea state conditions and air-sea fluxes during RaDyO," *J. Geophys. Res., Oceans*, vol. 117, no. C7, Jul. 2012, Art. no. C00H19, doi: 10.1029/2011JC007336.

[15] N. J. M. Laxague, C. J. Zappa, D. A. LeBel, and M. L. Banner, "Spectral characteristics of gravity-capillary waves, with connections to wave growth and microbreaking," *J. Geophys. Res., Oceans*, vol. 123, no. 7, pp. 4576–4592, Jul. 2018, doi: 10.1029/2018JC013859.

[16] F. J. Wentz and D. K. Smith, "A model function for the ocean-normalized radar cross section at 14 GHz derived from NSCAT observations," *J. Geophys. Res., Oceans*, vol. 104, no. C5, pp. 11499–11514, May 1999.

[17] A. Stoffelen, J. A. Verspeek, J. Vogelzang, and A. Verhoef, "The CMOD7 geophysical model function for ASCAT and ERS wind retrievals," *IEEE J. Sel. Topics Appl. Earth Observ. Remote Sens.*, vol. 10, no. 5, pp. 2023–2134, May 2017.

[18] A. G. Fore, S. H. Yueh, B. W. Stiles, W. Tang, and A. K. Hayashi, "On extreme winds at L-band with the SMAP synthetic aperture radar," *Rem. Sens.*, vol. 11, pp. 1093-1–1093-7, May 2019.

[19] P. A. Hwang, D. M. Burrage, D. W. Wang, and J. C. Wesson, "Ocean surface roughness spectrum in high wind condition for microwave backscatter and emission computations," *J. Atmos. Ocean. Technol.*, vol. 30, no. 9, pp. 2168–2188, Sep. 2013, doi: 10.1175/JTECH-D-12-00239.1.

[20] W. J. Pierson and L. Moskowitz, "A proposed spectral form for fully developed wind seas based on the similarity theory of S. A. kitaigorodskii," *J. Geophys. Res.*, vol. 69, no. 24, pp. 5181–5190, Dec. 1964.

[21] K. Hasselmann *et al.*, "Measurements of wind-wave growth and swell decay during the Joint North Sea Wave Project (JONSWAP)," *Deutsch. Hydrogr. Z., Suppl.*, vol. A8, no. 12, pp. 1–95, 1973.

[22] K. Hasselmann, W. Sell, D. B. Ross, and P. Müller, "A parametric wave prediction model," *J. Phys. Oceanogr.*, vol. 6, no. 2, pp. 200–228, Mar. 1976.

[23] M. A. Donelan, J. Hamilton, and W. H. Hui, "Directional spectra of wind-generated waves," *Phil. Trans. Roy. Soc. Lond.*, vol. A315, no. 1534, pp. 509–562, Sep. 1985.

[24] I. R. Young, "Directional spectra of hurricane wind waves," *J. Geophys. Res.*, vol. 111, no. C8, pp. C08020-1–C08020-14, 2006.

[25] P. A. Hwang, Y. Fan, F. J. Ocampo-Torres, and H. García-Nava, "Ocean surface wave spectra inside tropical cyclones," *J. Phys. Oceanogr.*, vol. 47, no. 10, pp. 2393–2417, Oct. 2017, doi: 10.1175/JPO-D-17-0066.1.

[26] P. A. Hwang, "Duration- and fetch-limited growth functions of wind-generated waves parameterized with three different scaling wind velocities," *J. Geophys. Res.*, vol. 111, no. C2, pp. 1–10, 2006, doi: 10.1029/2005JC003180.

[27] S. J. Katzberg and J. Dunion, "Comparison of reflected GPS wind speed retrievals with dropsondes in tropical cyclones," *Geophys. Res. Lett.*, vol. 36, no. 17, pp. L17602-1–L17602-5, Sep. 2009, doi: 10.1029/2009GL039512.

[28] S. J. Katzberg, J. Dunion, and G. G. Ganoe, "The use of reflected GPS signals to retrieve ocean surface wind speeds in tropical cyclones," *Radio Sci.*, vol. 48, no. 4, pp. 371–387, Jul. 2013, doi: 10.1002/rds.20042.

[29] S. Gleason, "Space-based GNSS scatterometry: Ocean wind sensing using an empirically calibrated model," *IEEE Trans. Geosci. Remote Sens.*, vol. 51, no. 9, pp. 4853–4863, Sep. 2013.

[30] S. Gleason *et al.*, "Study of surface wind and mean square slope correlation in hurricane ike with multiple sensors," *IEEE J. Sel. Topics Appl. Earth Observ. Remote Sens.*, vol. 11, no. 6, pp. 1975–1988, Jun. 2018, doi: 10.1109/JSTARS.2018.2827045.

[31] P. A. Hwang and Y. Fan, "Low-frequency mean square slopes and dominant wave spectral properties: Toward tropical cyclone remote sensing," *IEEE Trans. Geosci. Remote Sens.*, vol. 56, no. 12, pp. 7359–7368, Dec. 2018, doi: 10.1109/TGRS.2018.2850969.

[32] G. J. Komen, L. Cavaleri, M. Donelan, K. Hasselmann, S. Hasselmann, and P. A. E M. Janssen, *Dynamics and Modelling of Ocean Waves*. Cambridge, U.K.: Cambridge Univ. Press, 1994, p. 532.

[33] D. A. Drazen, W. K. Melville, and L. Lenain, "Inertial scaling of dissipation in unsteady breaking waves," *J. Fluid Mech.*, vol. 611, pp. 307–332, Sep. 2008.

[34] R. W. Burling, "The spectrum of waves at short fetches," *Deutsche Hydrographische Zeitschrift*, vol. 12, no. 3, pp. 96–117, May 1959.

[35] F. Dobson, W. Perrie, and B. Toulany, "On the deep-water fetch laws for wind-generated surface gravity waves," *Atmos.-Ocean*, vol. 27, no. 1, pp. 210–236, Mar. 1989.

[36] A. V. Babanin and Y. P. Soloviev, "Field investigation of transformation of the wind wave frequency spectrum with fetch and the stage of development," *J. Phys. Oceanogr.*, vol. 28, no. 4, pp. 563–576, Apr. 1998.

[37] H. García-Nava, F. J. Ocampo-Torres, P. Osuna, and M. A. Donelan, "Wind stress in the presence of swell under moderate to strong wind conditions," *J. Geophys. Res.*, vol. 114, no. C12, Dec. 2009, Art. no. C12008, doi: 10.1029/2009JC005389.

[38] F. J. Ocampo-Torres, H. García-Nava, R. Durazo, P. Osuna, G. M. Díaz Méndez, and H. C. Graber, "The INTOA experiment: A study of ocean-atmosphere interactions under moderate to strong offshore winds and opposing swell conditions in the Gulf of Tehuantepec, Mexico," *Boundary-Layer Meteorol.*, vol. 138, no. 3, pp. 433–451, Mar. 2011, doi: 10.1007/s10546-010-9561-5.

[39] P. A. Hwang, H. García-Nava, and F. J. Ocampo-Torres, "Observations of wind wave development in mixed seas and unsteady wind forcing," *J. Phys. Oceanogr.*, vol. 41, no. 12, pp. 2343–2362, Dec. 2011.

[40] C. W. Wright *et al.*, "Hurricane directional wave spectrum spatial variation in the open ocean," *J. Phys. Oceanogr.*, vol. 31, no. 8, pp. 2472–2488, Aug. 2001.

[41] E. J. Walsh *et al.*, "Hurricane directional wave spectrum spatial variation at landfall," *J. Phys. Oceanogr.*, vol. 32, no. 6, pp. 1667–1684, Jun. 2002.

[42] P. A. Hwang and E. J. Walsh, "Azimuthal and radial variation of wind-generated surface waves inside tropical cyclones," *J. Phys. Oceanogr.*, vol. 46, no. 9, pp. 2605–2621, Sep. 2016, doi: 10.1175/JPO-D-16-0051.1.

[43] T. Elfouhaily, B. Chapron, K. Katsaros, and D. Vandemark, "A unified directional spectrum for long and short wind-driven waves," *J. Geophys. Res., Oceans*, vol. 102, no. C7, pp. 15781–15796, Jul. 1997.

[44] C. Ruf, *CYGNSS Handbook*. Ann Arbor, MI, USA: Univ. of Michigan, 2016, p. 155.

[45] M. A. Donelan and W. J. Pierson, Jr., "Radar scattering and equilibrium ranges in wind-generated waves with application to scatterometry," *J. Geophys. Res. Oceans*, vol. 92, no. C5, pp. 4971–5029, May 1987.

[46] I.-J. Moon, I. Ginnis, T. Hara, H. L. Tolman, C. W. Wright, and E. J. Walsh, "Numerical simulation of sea surface directional wave spectra under hurricane wind forcing," *J. Phys. Oceanogr.*, vol. 33, no. 8, pp. 1680–1706, Aug. 2003.

[47] P. G. Black *et al.*, "Air-sea exchange in hurricanes: Synthesis of observations from the coupled boundary layer air-sea transfer experiment," *Bull. Amer. Meteorol. Soc.*, vol. 88, no. 3, pp. 357–374, Mar. 2007.

[48] Y. Fan, I. Ginis, T. Hara, C. W. Wright, and E. J. Walsh, "Numerical simulations and observations of surface wave fields under an extreme tropical cyclone," *J. Phys. Oceanogr.*, vol. 39, no. 9, pp. 2097–2116, Sep. 2009.

[49] Y. Fan and W. E. Rogers, "Drag coefficient comparisons between observed and model simulated directional wave spectra under hurricane conditions," *Ocean Model.*, vol. 102, pp. 1–13, Jun. 2016, doi: 10.1016/j.ocemod.2016.04.004.

[50] P. A. Hwang and Y. Fan, "Effective fetch and duration of tropical cyclone wind fields estimated from simultaneous wind and wave measurements: Surface wave and air–sea exchange computation," *J. Phys. Oceanogr.*, vol. 47, no. 2, pp. 447–470, Feb. 2017, doi: 10.1175/JPO-D-16-0180.1.

[51] P. A. Hwang and T. L. Ainsworth, "*L*-band ocean surface roughness," *IEEE Trans. Geosci. Remote Sens.*, vol. 58, no. 6, pp. 3988–3999, Jun. 2020, doi: 10.1109/TGRS.2019.2960130.

[52] P. A. Hwang, F. J. Ocampo-Torres, and H. García-Nava, "Wind sea and swell separation of 1D wave spectrum by a spectrum integration method," *J. Atmos. Ocean. Technol.*, vol. 29, no. 1, pp. 116–128, Jan. 2012, doi: 10.1175/JTECH-D-11-00075.1.

[53] P. A. Hwang and F. Fois, "Surface roughness and breaking wave properties retrieved from polarimetric microwave radar backscattering," *J. Geophys. Res., Oceans*, vol. 120, no. 5, pp. 3640–3657, May 2015.

[54] M. S. Longuet-Higgins, D. E. Cartwright, and N. D. Smith, "Observations of the directional spectrum of sea waves using the motions of a floating buoy," in *Ocean Wave Spectra*. Englewood Cliffs, NJ, USA: Prentice-Hall, 1963, pp. 111–136.

[55] H. Mitsuyasu *et al.*, "Observation of the directional spectrum of ocean waves using a clover-leaf buoy," *J. Phys. Oceanogr.*, vol. 5, no. 10, pp. 750–760, Oct. 1975.

[56] D. E. Hasselmann, M. Dunckel, and J. A. Ewing, "Directional wave spectra observed during JONSWAP 1973," *J. Phys. Oceanogr.*, vol. 10, no. 8, pp. 1264–1280, Aug. 1980.

[57] K. C. Ewans, "Observations of the directional spectrum of fetch-limited waves," *J. Phys. Oceanogr.*, vol. 28, no. 3, pp. 495–512, Mar. 1998.

[58] P. A. Hwang, D. W. Wang, E. J. Walsh, W. B. Krabill, and R. N. Swift, "Airborne measurements of the wavenumber spectra of ocean surface waves. Part II: Directional distribution," *J. Phys. Oceanogr.*, vol. 30, no. 11, pp. 2768–2787, Nov. 2000.

[59] P. A. Hwang and D. W. Wang, "Directional distributions and mean square slopes in the equilibrium and saturation ranges of the wave spectrum," *J. Phys. Oceanogr.*, vol. 31, no. 5, pp. 1346–1360, May 2001.

[60] I. R. Young and A. V. Babanin, "The form of the asymptotic depth-limited wind wave frequency spectrum," *J. Geophys. Res.*, vol. 111, no. C6, 2006, Art. no. C06031, doi: 10.1029/2005JC003398.

[61] I. R. Young and A. V. Babanin, "The form of the asymptotic depth-limited wind-wave spectrum: Part II—The wavenumber spectrum," *Coastal Eng.*, vol. 56, pp. 534–542, May 2009.

[62] I. R. Young and A. V. Babanin, "The form of the asymptotic depth-limited wind-wave spectrum: Part III—Directional spreading," *Coastal Eng.*, vol. 57, pp. 30–40, May 2010.

[63] D. R. Thompson, "Calculation of radar backscatter modulations from internal waves," *J. Geophys. Res.*, vol. 93, no. C10, pp. 12371–12380, Oct. 1988.

[64] D. R. Thompson, B. L. Gotwols, and R. E. Sterner, II, "A comparison of measured surface wave spectrum modulation with prediction from a wave-current interaction model," *J. Geophys. Res.*, vol. 93, no. C10, pp. 12339–12343, Oct. 1988.

[65] W. J. Plant, "The modulation transfer function: Concept and applications," in *Radar Scattering From Modulated Wind Waves*, G. J. Komen and W. A. Oost, Eds. Boston, MA, USA: Kluwer, 1989, pp. 155–172.

Paul A. Hwang received the B.S. degree in oceanography from National Taiwan Ocean University, Keelung, Taiwan, in 1973, the M.S. degree in ocean engineering from the University of Rhode Island, Kingston, RI, USA, in 1978, and the Ph.D. degree in civil engineering from the University of Delaware, Newark, DE, USA, in 1982.

After graduate schools, he had postdoctoral training at the Air-Sea Interaction Laboratory, University of Delaware for two and half years. He was a Staff Scientist with Ocean Research and Engineering, Pasadena, CA, USA, for four years, with Science and Technology, Hampton, VA, USA, for one year, and also with Quest Integrated, Inc., Kent, WA, USA, for five years. He joined Naval Research Laboratory, Washington, DC, USA, in 1995, first with the Oceanography Division from 1995 to 2006, and since 2006, he has been with the Remote Sensing Division. His research interests include spatial and temporal evolution of ocean surface waves, characteristics of ocean surface roughness, and hydrodynamic aspects of microwave and acoustic remote sensing of the ocean.